Carbon 165 (2020) 45–54

Contents lists available at ScienceDirect

Carbon

journal homepage: www.elsevier.com/locate/carbon

Porous graphite fabricated by liquid metal dealloying of silicon carbide

G. Greenidge , J. Erlebacher *

Department of Materials Science and Engineering, Johns Hopkins University, Baltimore, MD, USA

ARTICLE INFO

Article history:
Received 19 January 2020
Received in revised form
30 March 2020
Accepted 12 April 2020
Available online 16 April 2020

ABSTRACT

Porous graphite was prepared by dealloying SiC in molten germanium, and then excavating the Ge phase. Dealloying is a technique whereby nanoporous materials are produced via the selective dissolution of one or more components from a homogeneous alloy. Here, the liquid metal dealloying (LMD) process was extended to non-metal precursors, demonstrating that carbide-derived carbons (CDCs) can be fabricated by this process. The dealloying depth, concentration profile and length scale of the dealloyed microstructure were examined as they varied with immersion times and temperatures. The dealloying depth h varied with time as $h \sim t^{1/2}$ and we also observed a build-up of Si concentration in the germanium near the dealloying interface. These observations are consistent with kinetics that are rate-limiting in the liquid germanium side of the moving interface. However, the measured activation barrier of 2.4–2.8 eV was too high to be consistent with diffusion in the liquid phase, so instead we propose a mechanism in which Si diffusion is impeded by unsaturated carbon bonds near the dealloying interface. The porous graphite exhibited three-dimensional connectivity and a high degree of crystallinity, with an I(D)/I(G) ratio of 0.3 for samples dealloyed at the highest temperatures.

1. Introduction

Porous graphite is a versatile material with a wide range of applications. Depending on the details of its microstructure, its desirable properties include high specific surface area, good electrical conductivity and relatively low cost. Such characteristics make it useful for hydrogen adsorption [1], molecular sieves [2], filtration devices [3] and electrode materials in devices such as Li ion batteries [5,6] and capacitors [7]. Some traditional methods for synthesizing porous carbon materials involve high temperature catalytic or chemical activation, and carbonization of a precursor [8–10]. While various methods of synthesizing porous carbon materials exist, producing interconnected material with tunable pore sizes, narrow feature size distribution and a significant degree of graphitization has been a challenge. For these reasons, identifying new methods to transform carbon-containing materials into porous graphite is of significant scientific interest.

Porous graphite synthesis from carbides is a well-studied field and a comprehensive review of the topic can be found in Ref. [11]. Carbide-derived carbons (CDCs) employ a direct transformation of a carbide (SiC, VC, TiC etc.) to carbon using a variety of processing conditions that lead to differing properties and morphologies of the resulting material, including nanotubes, diamond, carbon onions and porous carbon with varying pore sizes [12–15]. The most common synthesis methods include halogenation, hydrothermal treatment and thermal decomposition. Halogen treatment is a process in which the metal or metalloid atoms in the carbide are selectively etched upon exposure to a halogen containing gas. The carbon fabricated by treatment in pure chlorine gas is predominatly highly disordered and porous, but often contains residual halogen or metal chlorides that can be removed by annealing [11,15]. Hydrothermal decomposition involves interaction of the precursor with hot, high-pressure water in the range of 200–1000 °C and pressures of up to hundreds of MPa. The carbon structure formed by this technique varies depending on the precursor and the processing conditions; for instance, amorphous porous graphite was grown on the surface of Tyranno fibers (amorphous SiO_xC_y with nanometer-sized β-SiC domains) at 300–400 °C and 100 MPa, whereas the formation of amorphous carbon, graphite and diamond structured carbon were reported on the surface of α- and β-SiC powder and single crystals after treatments at 300–800 °C and 100–500 MPa [11,16–19]. Thermal decomposition of carbides takes advantage of carbon's thermal stability to transform the carbide precusor into carbon in a vacuum or in high-temperature inert atmospheres [11]. Various carbon morphologies are also produced by this method, including graphene, nanotubes and porous carbon

* Corresponding author.
E-mail address: jonah.erlebacher@jhu.edu (J. Erlebacher).

https://doi.org/10.1016/j.carbon.2020.04.028
0008-6223/

[11,20,21].

Another, but less well-studied, technique previously used to fabricate nanoporous graphite is liquid metal dealloying (LMD). In its most general sense, dealloying is a processing technique wherein a homogenous non-porous alloy undergoes selective dissolution of one or more of its components under conditions where the remaining component re-organizes itself, usually via interfacial diffusion, into a three-dimensional bicontinuous porous structure. Because the final structure forms as a kinetic competition between the rate of material removal and the rate of material re-organization along the interface between the alloy and the dissolution medium, the length scale of the resultant microstructure is controlled dynamically, rather than being intrinsic to the parent alloy [22–25]. Furthermore, because mass transport is primarily via interface diffusion, there are no mechanisms to create defects like grain boundaries; the implication of this is that if one dealloys a single crystal, the final dealloyed material is a porous single crystal. We shall see, however, that dealloying of SiC does not fall neatly into this category because mass re-organization of carbon is accompanied by simultaneous chemical changes.

Dealloying has been studied for over a century [26], but primarily in the context of metal alloy corrosion. In this context, we call the technique electrochemical dealloying (ECD). Detailed kinetic and microstructural analysis by Pickering, Wagner and Forty [25,27,28] provided the basis for modern study; more recently, Erlebacher et al. recognized the utility of dealloying as a method to make bulk quantities of nanostructured materials [29]. Our understanding of ECD has become well-established, and leads to the following general model of microstructural evolution: in ECD of a two-component alloy [30], e.g. $Ag_{70}Au_{30}$, a common precursor, porosity evolution is driven by the application of a potential that lies between the reduction potentials of the two elements. Under these conditions, Ag atoms are easily solvated and extracted from low coordination sites, but the unoxidized Au atoms are mobile enough to diffuse along the solid-liquid interface to reorganize and form an open porous structure with 20–30 nm ligaments and pores [22,23,31].

Liquid metal dealloying (LMD) is analogous to ECD with a few notable differences. In LMD, the dissolution medium is a liquid metal and the driving force for selective dissolution is differences in enthalpy of mixing between the alloy and the liquid metal. The process was first described by Wagner [32] over 50 years ago but has recently re-emerged after work published by Kato and Wada [33]. In LMD, a homogeneous alloy is submerged into a molten metal whose enthalpy of mixing is positive with respect to the remaining species and negative with the dissolving species, i.e., one species dissolves and the other does not. As in ECD, the non-dissolved species migrates along the alloy-melt interface and re-organizes into a porous structure. But upon termination of the process, pulling the alloy out of the melt, the molten metal simply solidifies and a fully dense composite is formed that consists of the porous material with the dissolving medium solidified within the pores. This bicontinuous nanocomposite sometimes exhibits superior mechanical properties [31,34]. However, if a porous monolith is preferred, the dissolving metal can be excavated by chemical etching.

The reintroduction of LMD has proven to be a significant advancement to the wider field of dealloying because it expands the set of materials systems to study when compared to ECD [31]. The electrochemistry of precious metals is well understood but less noble metals rapidly oxidize or corrode in aqueous solvents, placing limitations on the set of materials that can be electrochemically dealloyed. In contrast, by using a liquid metal as the dissolution medium, a variety of new single and multi-component porous materials have been fabricated, e.g. porous Ta from Ta–Ti dealloyed in molten Cu [35], porous Nb/Nb_5Si_3 composite also dealloyed in molten Cu [36] and porous Si from Mg–Si dealloyed in molten Bi [37]. Most systems studied by LMD utilize metal alloy precursors but it has recently been demonstrated that nanographite can be fabricated by selectively dissolving the metal from a metal-carbon precursor. Specifically, Yu et al. began with a Mn–C powder precursor ($\leq$100 μm) and selectively dissolved Mn in molten Bi to form a three dimensional nanoporous graphite powder [38].

The structure of the resulting carbon material produced via either LMD or CDC formation can be affected by the concentration of carbon in the precursor. SiC and Ti_3SiC_2 produce CDCs with varying porosities due to differences in the carbon fraction [11]. A similar phenomenon is found for the LMD of metals. Geslin et al. reported a wide range of porous Ta morphologies fabricated by dealloying Ti_xTa_{1-x} with varying phase fractions of the non-dissolving component, from the prototypical bicontinuous morphology at high Ta mole fractions (35 at.%) to a lamellar structure at intermediate concentrations (15 at.%) [39]. Additionally, two distinct graphite morphologies were observed from the LMD of a $Mn_{85}C_{15}$ precursor that phase separated into $Mn_{23}C_6$ and α-Mn, where the lower porosity material originated from the former phase [38]. We also suspect variations in the morphology of resultant carbon produced via LMD of metals and ceramics due to differences in crystal structure. Since covalent bonding is directional and the crystal structure of the ceramic is less densely packed than its metallic counterparts, we can expect differences in the connectedness and morphologies of the porous materials produced when one of the components is extracted.

In this work, we demonstrate for the first time the LMD technique on a ceramic precursor, further adding to the set of materials systems amenable to dealloying. Porous graphite was fabricated by immersion of SiC in molten Ge, where Si was selectively dissolved from the precursor. The system exhibits the required thermodynamic requirements for dealloying, namely, carbon is insoluble in Ge while Si and Ge are miscible over their entire composition range both in the solid and liquid phases. However, compared to other dealloyed systems, SiC is unique being a covalently bonded stoichiometric precursor with a very high bond enthalpy and upon dealloying carbon transforms from an sp^3 bonded network with Si to a highly crystalline sp^2 bonded network without a further graphitization step; it is a kind of LMD with an additional chemical (structural) reaction at the metal/solid interface.

Here we report the preparation and characterization of dealloyed 4H–SiC single crystals. No other SiC polytype was used to elucidate the kinetics of dealloying, but this polymorph may be used as a prototype for the dealloying of other SiC crystal structures as well as other intermetallics. We find that SiC can be dealloyed in molten Ge to produce a carbon-Ge composite that retains the dimensions, though not the crystal orientation, of the parent material. We also find that the dealloying kinetics in this system exhibit most, but not all, of the characteristics of LMD in all-metal alloy systems. For instance, the dealloying depth h slows down as a function of time t as $h \sim t^{1/2}$ which is typical behavior in the LMD of metal containing alloys. Unlike conventional liquid metal dealloying, however, the crystal structure of the parent material is not preserved, and we transform single crystal SiC to a polycrystalline graphitic network with a generally uniform length scale. Ge can be chemically etched from dealloyed SiC to expose the interconnected porous graphite film, and this material exhibits a characteristic pore size depending on the processing temperature.

1.1. Experimental methods

The dealloying process is depicted in Fig. 1(a). Experiments were performed by submerging bulk SiC wafer pieces into molten Ge. To elucidate the kinetics of dealloying in this system, we examined the

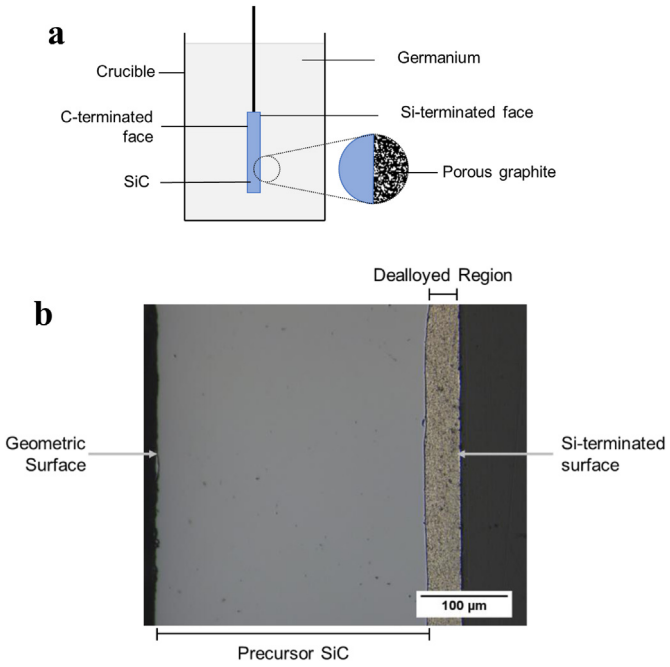

Fig. 1. (a) Schematic diagram depicting dealloying process of single crystal SiC in molten Ge. Ge dissolves Si from the parent alloy, leaving behind a porous graphite network. (b) Optical micrograph showing SiC with a dealloyed region. Ge, the dissolving medium, solidifies in the carbon pores upon termination of the dealloying process. A fully dense network of carbon with Ge solidified in its pores is shown. Dealloying generally starts preferentially on the Si-terminated surface while the C-terminated surface remains unchanged. (A colour version of this figure can be viewed online.)

dealloying depth, concentration profile and characteristic size of the dealloyed microstructure as they varied with immersion times and temperatures.

In a typical experiment, a 20 g mass of *n*-doped germanium (99.999 wt% from Kurt J. Lesker) was inductively heated to fixed temperatures in a graphite crucible using a 4.5 kW Ambrell EkoHeat power supply. The chosen temperatures were 1200 °C (±25°), 1300 °C (±20 °C) and 1400 °C (±15 °C) and temperature measurements were made using an Ircon Modline 5 infrared camera with a Yokogawa controller. All experiments were carried out under a flowing Ar atmosphere (99.999 at. %). In a typical experiment, a single piece of research grade, *n*-doped SiC wafer (MSE Supplies) approx. 30 mm × 10 mm x 0.35 mm was immersed into molten Ge for varied times at the preset temperatures using a vacuum manipulator arm. Upon conclusion of each experiment, the sample was lifted out of the bath to initiate cooling and discontinue the dealloying process. Dealloying immersion times varied from 1 min to 9 min, cooling of samples occurred on the order of 1 s, and we assume that dealloying terminated once the sample was pulled from the dealloying bath. The result was a fully dense structure that consisted of porous graphite impregnated with a solid germanium/silicon composite.

Once prepared, dealloyed samples were mounted on their shortest dimension and polished through their cross-sections. A typical sample is shown in Fig. 1(b). We observed that SiC preferentially dealloyed on the Si-terminated face (see Discussion), and the present work only investigates the kinetics of dealloying on this surface. In approximately 10% of the samples, no dealloying was observed and in 25% of experiments, the dealloyed interfaces were neither sharp nor continuous. We believe this variation was likely due to surface contamination [40]. Most samples displayed a sharp and straight interface for a minimum length of 500 μm, and these samples were used for subsequent characterization. A minimum of 20 measurements from different regions of a sample were averaged to determine dealloying depth. Fig. 2 depicts a typical cross-section and corresponding dealloying depth measurements, assessed by measuring the length from the geometric surface of a sample to the planar dealloyed interface using ImageJ. Average ligament diameters were determined using the AQUAMI software [41] on SEM micrographs. Compositional analysis as a function of depth was performed using energy dispersive spectroscopy (EDS).

To excavate the carbon phase in the dealloyed samples, the Ge rich phase was dissolved in hot aqua regia for ~45 min and rinsed thoroughly in distilled water. The structure of the resulting porous graphite was then analyzed using a Horiba LabRam Evolution Raman microscope with a 532 nm laser. A Thermo Scientific Helios G4 UC Focused Ion Beam/Scanning Electron Microscope (FIBSEM) instrument equipped with an energy dispersive spectroscopy (EDS) detector was used to image the material and prepare carbon samples for imaging using the Thermo Scientific TF30 Transmission Electron Microscope (TEM).

Because bulk SiC wafers were used to obtain the kinetic parameters such as dealloying depth and ligament size, the form factor of the material we obtained after dealloying was a porous graphite film impregnated with solid Ge on the SiC surface. Obtaining a free-standing porous graphite membrane for further analysis proved to be experimentally challenging. As a method to produce large quantities of material suitable for functional analysis (such as BET surface area), we propose employing the use of SiC powder in future experiments which would circumvent this experimental limitation.

2. Results and discussion

2.1. General observations

In conventional dealloying experiments, the surfaces of the material are chemically identical and therefore dealloy in an identical fashion under the same conditions. However, single crystal SiC is bipolar with a Si (0001) face and a C ($000\bar{1}$) face and studies have reported markedly different chemical and physical properties of the two surfaces; for example, Kusunoki et al. found that after heating SiC at 1700 °C in a vacuum, an aligned carbon nanotube film grew on the C face perpendicular to the surface while multiple graphene sheets formed on the Si face under the same conditions [42,43]. In our experiments, we observed that the dealloying process is initiated more readily on the Si surface. This observation held especially at the lower dealloying temperatures; at higher processing temperatures, we more frequently observed the evolution of a porous carbon structure initiated on the C-terminated surface. We hypothesize that the high solubility of Si in Ge allowed for more effective wetting of the Si surface by Ge compared to the C terminated face, facilitating initiation of the dealloying reaction at the Si surface at lower temperatures.

The dealloying interface (i.e., the boundary between the dealloyed and undealloyed material) was sharp, continuous and obvious, as is clear from Fig. 1. Dealloying depth measurements were taken from dealloyed regions that had an interface length of 500 μm or longer where, in comparison, the ligament size of the porous carbon was on the order of tens of micrometers or less. Upon termination of the experiment, polished cross-sections show Ge solidified in the pores of the carbon and the carbon phase clearly appearing as dark precipitates dispersed throughout the lighter Ge background when examined via scanning electron microscopy.

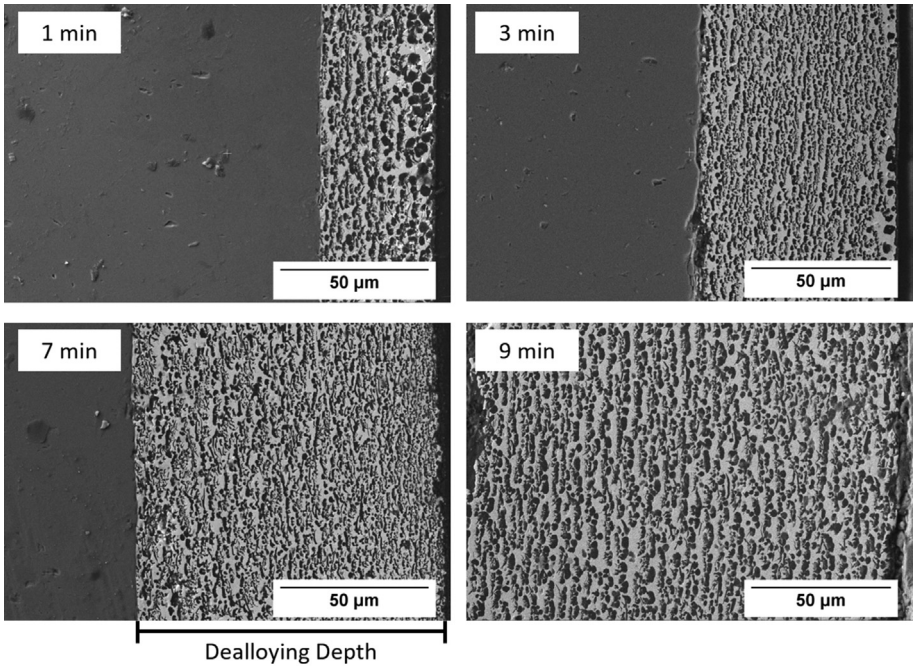

Fig. 2. Scanning electron microscopy (SEM) micrographs of SiC samples dealloyed in molten germanium at 1300 °C for different times. The dealloying front proceeds right to left from the geometric surface towards the sharp and flat dealloying interface. The dealloying region displays different contrast as the light phase is Ge rich and the dark phase is carbon. The two images on the left were taken at 850× magnification and the images on the right were taken at 800× magnification, but it can be observed that the dealloying depth increases with time.

2.2. Dealloying kinetics and morphological evolution in SiC-Ge

To discuss our observations regarding the dealloying kinetics of SiC in Ge, it is useful first to review the kinetic response during LMD to that of electrochemical dealloying (ECD), the latter of which uses an electrolyte to induce selective dissolution, in order to compare the behavior of SiC dealloying to both.

LMD and ECD are both corrosion processes that result in a bicontinuous microstructure, and a detailed comparison/contrast between the two techniques has been reviewed by McCue et al. [30]. Notable points for comparison between the methods are the rate-limiting kinetics and the solubility of the remaining component in the bath. In the systems examined to date, LMD exhibits a dealloying depth that increases with time as $t^{1/2}$, with a corresponding decrease in the interface velocity as the dealloyed front penetrates into the sample. In the Ti-Ta system dealloyed in molten copper, these observations were quantitatively consistent with diffusion-limited transport of Ti through the molten copper in the pores formed behind the moving dealloying front. In contrast, the dealloying depth in ECD shows a constant velocity [44], which indicates that the dealloying kinetics are limited by the interface dissolution reaction. The diffusion rates of the removed material in the liquid dissolution medium in both cases are similar, with diffusion coefficients of approximately 10^{-6} cm^2/s, so the difference in kinetics is primarily manifested in the interface velocity. Consistent with rate limiting behavior, for LMD, the dealloyed front typically advances at a velocity of order 1 μm/s whereas in ECD the interface velocity is of order 0.01 μm/s. Diffusion limited transport in LMD leads to a significant concentration (>10 at. %) of the dissolved species in the liquid medium near the dealloyed interface (within the porous layer) that decays toward the geometric surface of the sample.

SiC dealloyed in Ge exhibits kinetic behavior most similar to LMD. Fig. 3 shows the dealloying depth as a function of time for single crystal SiC at three different temperatures: 1200 °C, 1300 °C and 1400 °C. Similar to observations of dealloying of metallic systems, dealloying depth h increases with temperature for a fixed dealloying time t and varies as a power law relationship with time consistent with diffusion-limited kinetics, i.e., $h \sim t^{1/2}$. We were unable to find a value in the literature for the diffusivity of Si in molten Ge, so we assumed that, because both Si and Ge are Group IV elements, they are chemically similar and exhibit comparable diffusion behavior [45]. We therefore estimate the diffusion coefficient of Si in liquid Ge to be on the order of 10^{-4} cm^2/s based on the reported value for the self-diffusion coefficient of Ge in molten Ge as 1.8×10^{-4} cm^2/s at 1247 °C [46]. We find experimentally that the interface velocity in this system is of order 0.1-1 μm/s. Compared to typical ECD and LMD systems, diffusion of Si in the germanium bath

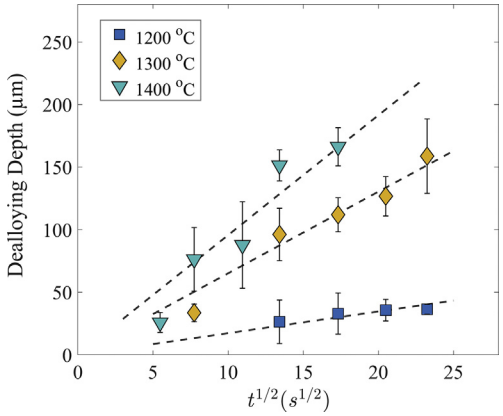

Fig. 3. Dealloying depth vs. $t^{1/2}$ for samples studied. We studied three temperatures: 1200 °C (blue, squares), 1300 °C (yellow, diamonds), and 1400 °C (green, triangles). Dealloying depth increased with increasing temperature and followed a power law relationship with time. The error bars represent one standard deviation. (A colour version of this figure can be viewed online.)

is approximately 2 orders of magnitude faster than in either ECD and LMD, while the interface velocities lie in-between typical values for the two processes. Because diffusion is relatively fast compared to the interface velocity, we found it surprising that the interface velocity exhibited apparent diffusion limited kinetics (i.e., slowed down with dealloying depth).

To examine the origin of rate-limiting behavior in more detail, we extracted the activation barrier associated with dealloying from our data collapse following the methodology outlined in Reference [35]. If there is an activated process controlling the dealloying kinetics, then dimensional analysis requires that any function such as the dealloying depth h must have the functional form $h(kt)$, where the Arrhenius rate constant is $k \sim \exp(-E_a/k_BT)$; k_B is Boltzmann's constant, T is the temperature and E_a is the activation barrier. To find E_a, then we plot $h(t)$ vs. scaled time $t' = t \cdot \exp(-E_a/k_BT)$, and optimizing for the best data collapse assuming, as is common, that $h(t)$ follows a simple power law relationship $h(t) \sim t^n$ (e.g., $h(t) \sim t^{1/2}$ for diffusion-limited kinetics). This requires varying both E_a and n (and a constant prefactor). Forcing $n = 0.5$ yields a reasonable fit to the data collapse as is shown in Fig. 4, for which $E_a = 2.8$ eV. The best data collapse using this approach, however, is achieved when $n = 0.67$ which yields a slightly smaller activation energy, $E_a = 2.4$ eV. It should be noted, however, the data collapse is relatively insensitive to this value. Either way, a value of E_a between 2.4 and 2.8 eV is unreasonably large for a liquid phase diffusion process. For comparison, the activation energy for self-diffusion in molten Ge is only 0.16 eV [46]. Our measured value is closer to solid-state diffusion in Si–Ge, for which the activation barriers range from 2.9 to 3.5 eV depending on composition [47]. Lee et al. reported on the kinetics of carbon formation via the chlorination of SiC and observed a similar anomaly: the CDC layer thickness followed a power law relationship with time where $n = ½$, but the calculated $E_a = 1.7$ eV was too high to be consistent with gas phase diffusion in the pores. Instead, an alternative mechanism of transport was suggested where chlorine diffused as an adsorbent on the pore surfaces [48].

We also examined the concentration profile of silicon as it varied through the dealloyed region by direct measurement of the solidified Ge-rich phase using EDS. As shown in Fig. 5, we found that the Si concentration profile decays away from the dealloying front, but the build-up of Si atoms only occurs in the first micrometer of a sample in a dealloyed region that extends to ca. 100 μm; after this first micron, the concentration of Si is below the EDS detection limit. In contrast, in the concentration profile obtained by McCue in the Ti–Ta system, the Ti concentration only reached a near-zero concentration close to the geometric surface of the dealloyed sample [35]. We were also unable to fit the concentration decay to McCue's model.

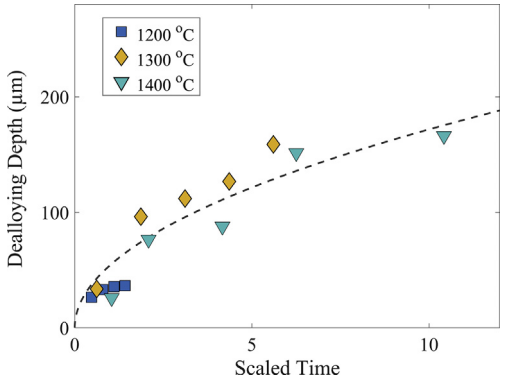

Fig. 4. Collapsed dealloying depth versus scaled time $t' = t \cdot \exp(-E_a/k_BT)$ for SiC for measurements taken at 1200 °C (blue, squares), 1300 °C (yellow, diamonds), and 1400 °C (green, triangles). Dashed line: fits to the data using the relationship $h(t) \sim t^{1/2}$. The values for E_a and the scaling exponent were determined as the values associated with best least-squares fit. (A colour version of this figure can be viewed online.)

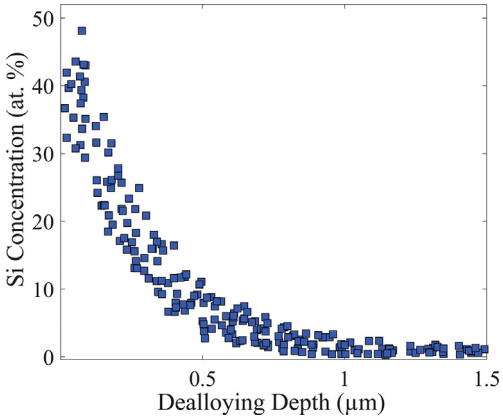

Fig. 5. Si concentration versus distance away from the dealloying interface for SiC dealloyed in molten Ge. Unlike in conventional LMD where there is a gradual decline of the dissolving component across the dealloyed region, the Si concentration declines rapidly to near 0 at. % within the first micrometer of the dealloyed region. (A colour version of this figure can be viewed online.)

The observations of (i) a high activation barrier associated with rate-controlling behavior, (ii) a slowdown of the interface velocity with time, and (iii) a decaying concentration of Si in the Ge liquid dealloying medium near the dealloying front, taken together, suggest that the mechanism of dealloying is complex. One possibility is a facile dissolution of a Si–C complex from the parent alloy that acts as a vehicle transporting C atoms to growing graphite clusters. This coupled species dissociates over approximately the first micron of the liquid, freeing Si to quickly diffuse into the molten Ge. A second possibility is that as carbon reorganizes from the sp^3 configuration in SiC to sp^2 hybridized graphite, there is a transition zone in which a high number of C-dangling bonds act as transient points of attachment for Si, significantly slowing down diffusion within this zone. Such novel chemical-limiting steps in dealloying kinetics may be unique to systems such as SiC where the hybridization of carbon changes during dealloying.

We briefly compare the kinetic response of carbon fabricated by LMD and halogenation, a conventional method of CDC preparation. In 2001, Ersoy and colleagues reported a linear growth rate for porous carbon films produced via halogenation of sintered SiC at 1000 °C [51]. Similarly to ECD, this relationship indicates an interface-limited reaction, where in the case of the CDC, the controlling factor of the reaction was not diffusion of the reactant species through the growing carbon film. The composition of the mixture affected the linear rate constant, but as an example, the linear rate constant for a chlorine-hydrogen environment was 0.03 μm/min. However, Lee et al. demonstrated faster kinetics and a diffusion-limited process for CDC growth in the same temperature range as Ersoy's study, but attributed the conflict to differences in experimental setup and procedures [48]. Regardless, the reaction kinetics described in both the interface and diffusion limited CDC growth processes are significantly slower than in LMD. According to Lee's study, growth of a 50 μm CDC film would take almost 5 h at 1000 °C (interface velocity of 0.2 μm/min). In the LMD process described in this work, the processing time to grow a porous graphite layer of equal thickness is only 15 min at 1200 °C (interface velocity of 3 μm/min).

2.3. Ligament morphology and size

Fig. 6(a) shows representative SEM micrographs of polished, cross-sectioned samples dealloyed at different temperatures. In each micrograph, the dark phase is carbon and the light phase is solidified germanium. For samples dealloyed at 1200 °C, the carbon phase presents as randomly oriented elongated spines with a high degree of interconnectedness. For samples dealloyed at 1300 °C, the carbon appears as circular particles aligned normal to the dealloying direction with much less interconnectivity. At the highest temperature examined, the anisotropy is reduced and the morphology consists primarily of disconnected circular structures interspersed in the Ge matrix. Even when the Ge phase was dissolved, the porous carbon appears as randomly oriented individual flakes and clusters of flakes on the surface (see Fig. 7) as opposed to a porous network. It is interesting to note that although the material does not appear to contain a high degree of interconnectivity in the SEM micrographs, the porous graphite was mechanically robust, surviving the vigorous etching and rinsing process, while still retaining the dimensions of the parent dealloyed zone. The TEM images (Fig. 8) of porous graphite processed at the highest temperature, 1400 °C, explain the inconsistency. The material consists of a network of ligaments that extend three-dimensionally; the ligaments are comprised of a series of overlapping graphite crystals which act as nodes from which elongated crystals branch. These ~1 μm long spokes connect various hubs; the result is a robust network that extends throughout the bulk of the

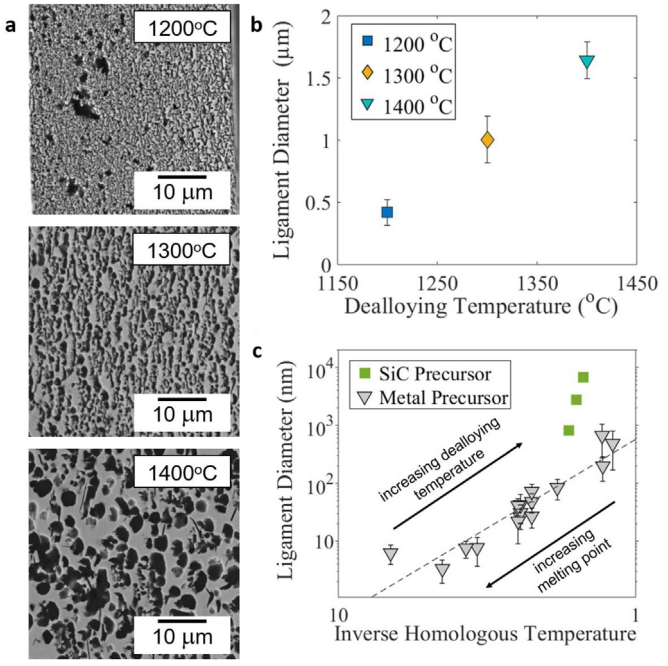

Fig. 6. (a) SEM micrographs depicting ligament size increase with increasing temperature. Variation in ligament morphology is also observed with a higher degree of interconnectedness at the lowest experimental temperature, coalesced graphite particles aligned perpendicular to the dealloying direction at 1300 °C and larger circular particles at the highest temperature. (b) Ligament diameter versus processing temperature for dealloying SiC. Length scales increase at higher temperatures. (c) Trend in ligament diameter versus inverse homologous temperature ($T_m/T_{dealloy}$) for electrochemical dealloying and liquid metal dealloying at different times, shown as grey triangles for metal systems (adapted with permission from Ref. [30]. Error bars represent one standard deviation. For comparison, the trend between ligament diameter and inverse homologous temperature for SiC ($T_{sublimation}/T_{dealloy}$) is shown as green squares. Error bars lie within the data markers. (A colour version of this figure can be viewed online.)

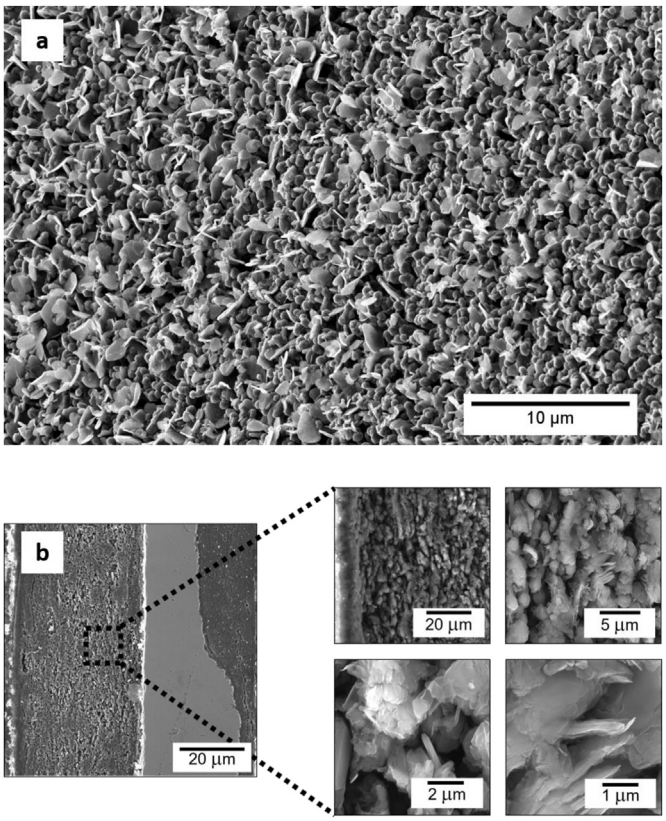

Fig. 7. (a) SEM micrograph of porous graphite produced by dealloying at 1400 °C. (b) SEM micrograph of a cross-section of SiC dealloyed at 1300 °C. The morphology of the porous graphite is shown at increasing magnifications. The material presents as of clusters of graphite flakes on the surface.

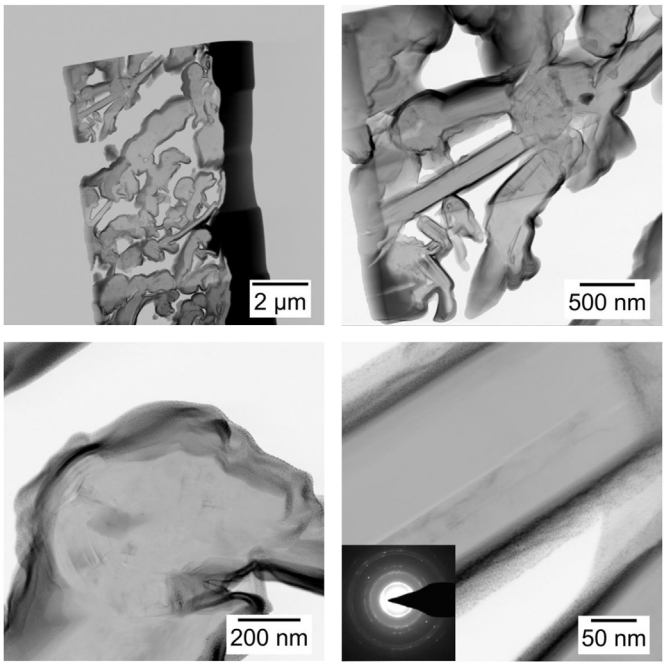

Fig. 8. TEM images of a SiC sample dealloyed in molten Ge at 1400 °C after etching in aqua regia to remove solidified Ge from pores. Images depict highly interconnected porous graphite. (Inset) selected area electron diffraction shows that the graphite is polycrystalline.

material to form a topologically connected porous structure that we were unable to visualize with SEM.

We used the Aquami software on images of the porous graphite-germanium composite produced after dealloying (see Fig. 6 (a)) to quantify the ligament sizes and an explanation of the detailed methods used in the digital image analysis can be found in Reference [41]. The ligament morphology of dealloyed SiC differs from those produced in conventional dealloying but in a general sense, the relationship between ligament length scale and temperature is maintained as shown in Fig. 6(b). Specifically, the ligament length scale grows with increasing temperature. Looked at in detail, however, there is an interesting discrepancy associated with the remaining component being carbon. Sieradzki, McCue, et al. determined that ligament diameter scales with "inverse homologous temperature," $T_m/T_{dealloy}$, for both LMD and ECD [30,52]. A plot showing this relationship is depicted in Fig. 6(c) where data from the present work is also shown for comparison. Since graphite does not melt at atmospheric pressure, its sublimation point, 3642 °C, was used to calculate the inverse homologous temperature. While we do observe an increase in ligament length scaled with inverse homologous dealloying temperature, our work does not fall on the expected universal trend for LMD and ECD. We attribute this discrepancy to the substitution of melting point with sublimation point and the larger ligament length scale observed for the SiC system.

Using images from Reference [38], we calculated ligament diameters of the porous graphite produced by LMD of a Mn–C precursor at 800 °C to be approximately 0.2 μm. In comparison, our samples processed at the lowest temperature (1200 °C) developed ligament diameters less than 0.5 μm. We posit that by reducing the processing temperature even further, we can evolve a material with even higher porosity. We mentioned earlier in the manuscript that we observed limited wetting of the SiC by the liquid metal at temperatures lower than 1200 °C but the literature suggests that we can alter the composition of the Ge bath to improve the surface attraction between the materials [53], allowing us to probe even lower temperature ranges in the future.

Due to decreased surface mobility, materials with higher melting points produce smaller ligaments after dealloying. During dealloying, the material behind the dissolution front often coarsens, and this is the reason larger ligament sizes are seen at the outer geometric surface of a sample. Coarsening is driven by two surface-diffusion mediated processes with a $t^{1/4}$ dependence: capillary effects and genus-reduction events. The driving force in the former is a reduction of surface area where there is mass transport from regions of high to regions of low curvature. The latter is driven by Rayleigh instabilities where ligaments pinch off to reduce the genus or number of handles on a ligament [54]. In metal systems, experiments show a significant gradient of coarsening within a single sample; the ligament size varies by almost three orders of magnitude across the dealloyed depth. Gaskey et al. developed a model to describe the observed phenomenon [36]. They explain that coarsening in nanoporous metals is dominated by an attachment-mediated Ostwald ripening process that is facilitated by the solubility of the remaining component in the melt. In contrast, the feature sizes in our experiments are – for the most part – uniform across the dealloyed region at lower dealloying temperatures, indicating essentially zero carbon interface mobility (and consistent with the consolidation of the carbon network near the dealloying front). However, at 1300 °C, we sometimes observed regions with an abrupt size increase and a transition from a filamentous to a large-scale morphology near the surface of the sample (Fig. 9), which we are unable to explain at this point.

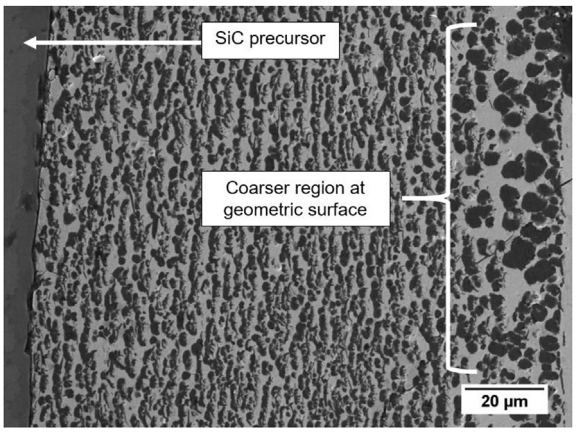

Fig. 9. SEM micrograph showing anomalous carbon structures with larger feature size near the geometric surface of the sample after LMD at 1300 °C. There is a 25 μm region on the surface where the carbon ligaments appear >5 μm in diameter, but the rest of the sample shows uniform particle size up to the dealloyed interface.

2.4. Raman spectroscopy of porous graphite

The Ge rich phase of dealloyed SiC was chemically etched in hot aqua regia and the presence of porous carbon was confirmed via EDS analysis, selected area electron diffraction and Raman spectroscopy. The Raman fingerprint of graphite-related materials exhibit three prominent peaks: the G band (~1580 cm^{-1}), D (~1350 cm^{-1}) and the 2D band (~2700 cm^{-1}). The G peak is activated by sp^2 carbon networks and is therefore always present in the Raman fingerprint of any graphitic material, along with the 2D band which corresponds to a high energy second order-process and is also always observed in the fingerprint. The D band and the D' band (1620 cm^{-1}) are defect activated peaks and are weak in the Raman spectra of graphite with low defect concentrations [55–57]. The ratio of intensity between the D and G peaks, the I(D)/I(G) ratio, can provide information about the crystal size and the defect density in the material where this ratio is inversely proportional to the crystal size, L_A [55]. The shape of the 2D band and the I(2D)/I(G) ratio can be used to identify the number of graphene layers [58]. Fig. 10 demonstrates a typical Raman spectrum of the material

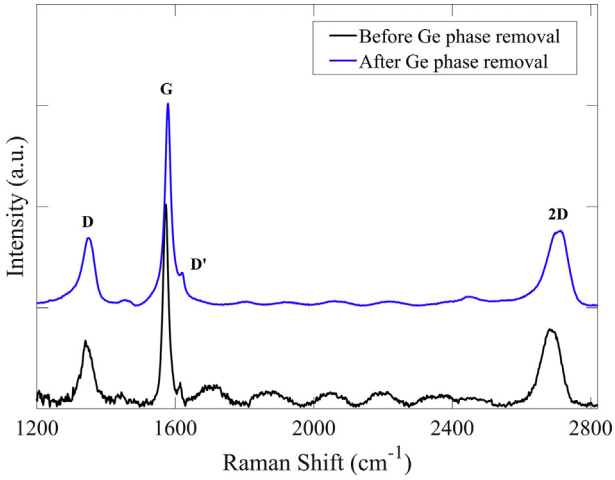

Fig. 10. Raman spectra of the porous graphite before and after the Ge phase was etched from the pores. The Raman fingerprint exhibits characteristic features of nanographite. The very low intensity peaks between 1700 cm^{-1} and 2600 cm^{-1} were activated by epoxy sample mount.

prepared at 1400 °C. The Raman features shown in the present work are similar to those reported for nanocrystalline graphite [57], that is, graphite that consists of small, randomly oriented crystallites in which the many grain boundaries and edges strongly activate the defect peaks. In order to evaluate the effect of the Ge removal from the graphite pores, Raman analysis was performed on material before and after Ge etching, which is also depicted in Fig. 10. We observed G band broadening by 6 cm^{-1} and a stiffening of peaks after Ge removal where the G peak shifted by 5 cm^{-1}. Such small changes in the peaks are consistent with strain and doping by metals, which are known to influence the Raman spectrum of graphene and graphite [59–61]. However, the I(D)/I(G) and I(2D)/I(G) ratios remain relatively unchanged, indicating that no significant change in the graphite structure occurred during the corrosion of Ge in aqua regia.

We also analyzed the Raman spectra of graphite produced by dealloying at different processing temperatures and the results are shown in Fig. 11 and summarized in Table 1. For graphite fabricated by dealloying at lower temperatures, the full width at half maximum (FWHM) of the G peak broadened due to increased disorder [62]. The crystallite size, L_A, was computed using the general equation [57,63]:

$$L_A\left(nm\right) = \left(2.4x10^{-10}\right)\lambda_{laser}^{4}\frac{I(D)^{-1}}{I(G)}$$

As expected, we observed an inverse relationship between processing temperature and I(D)/I(G) ratio, an indicator for crystallinity. This trend suggests that we can tune the degree of disorder and crystallite size by varying the temperature.

We compare the Raman features of porous graphite produced in this work to that of carbon black (Cabot Corporation). Despite its low surface area, carbon black's moderate conductivity, low cost and large pore volume make it an attractive material for electrocatalyst support in fuel cells and as a component of the cathode in lithium ion batteries [64]. However, scientists have been looking for carbon black substitutes that exhibit superior conductivity, crystallinity and durability. Since Yu reported decreased volume resistivity in the porous graphite material post-graphitization at high temperatures, we note the implied relationship that a lower I(D)/(I(G) ratio (higher crystallinity) indicates increased conductivity [38]. In this work, porous graphite synthesized from the LMD of SiC at 1200 °C had an I(D)/I(G) ratio of 0.41. In comparison, the measured I(D)/I(G) ratio of carbon black was 0.78, whereas the 3D porous graphite produced via

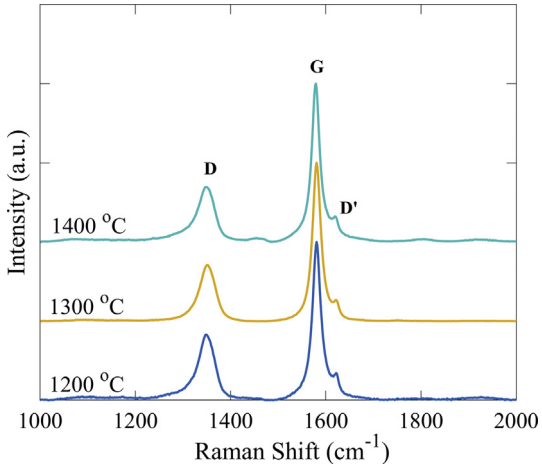

Fig. 11. Raman spectra of porous graphite processed at different dealloying temperatures. (A colour version of this figure can be viewed online.)

Table 1
Summary of properties of porous graphite processed under different conditions.

	1200 °C	1300 °C	1400 °C	1400 °C Ge in Pores	Carbon Black
I(D)/I(G)	0.41	0.36	0.34	0.33	0.78
L_A (nm)	46.7	53.9	57.4	58.9	24.6
FWHM-G (cm^{-1})	21.3	21.0	20.2	26.2	51.8
G Peak (cm^{-1})	1580.6	1580.7	1578.8	1574.1	1585.2

LMD in Yu's work from a Mn–C precursor exhibited an I(D)/I(G) ratio of 0.46 only after a secondary high temperature graphitization step that involved heating the material at 1500 °C for 2 h [38]. CDCs fabricated by halogenation are predominantly amorphous even in material prepared at temperatures over 1000 °C; for example, Ersoy reported I(D)/(I(G) ratios of ~1 for CDCs fabricated by chlorination [15,51,65,66]. The as-prepared porous graphite fabricated in this study exhibited a high degree of crystallinity compared to material prepared by other methods, which augurs well for its use in electrical devices.

3. Conclusion

We report the fabrication of a porous network of graphite via the liquid metal dealloying (LMD) of a covalently bonded ceramic precursor, SiC, in molten germanium. This work focuses on the fundamental kinetics of a promising technique whereby mechanically robust and highly crystalline porous graphite can be produced. Preparing porous graphite via the LMD of SiC provides an alternative and facile route of preparing a CDC with a uniform morphology, tunable ligament sizes, narrow size distributions, fast kinetics and low defect density indicated by I(D)/I(G) ratios as low as 0.3. Furthermore, no additional annealing step is required to remove residual halogen adsorbents. With respect to dealloying generally, our process expands the set of systems that are suitable candidates for liquid metal dealloying. When compared to previous work on fabrication of porous graphite via LMD, our as-prepared material exhibited greater uniformity and superior crystallinity, despite having larger pore sizes which we attribute to the higher processing temperatures.

The kinetics of LMD of the non-metal containing SiC precursor was examined by varying the dealloying time and temperature, and the kinetics were compared to that of conventional dealloying and CDC processing. It was found that the interface velocity in the present work is much faster than in CDC formation via chlorination but slower than in conventional LMD. Regardless, diffusion-limited kinetics dominate in all three processes. The concentration gradient of Si decayed away from the dealloying interface and the dealloying depth h varied with time as $h \sim t^{1/2}$, associated with rate-limiting diffusion away from the interface. However, the measured activation barrier of 2.4–2.8 eV is too high to be consistent with diffusion in the Ge melt, so instead we propose a complex mechanism in which Si diffusion is impeded by unsaturated carbon atoms near the dealloying front.

Declaration of competing interest

The authors declare that they have no known competing financial interests or personal relationships that could have appeared to influence the work reported in this paper.

CRediT authorship contribution statement

G. Greenidge: Formal analysis, Writing - original draft. **J. Erlebacher:** Formal analysis, Writing - original draft.

Acknowledgments

This work was supported by the National Science Foundation under grant DMR-1806142. The authors would like to thank Ian McCue for helpful discussions.

References

[1] X.B. Zhao, B. Xiao, A.J. Fletcher, K.M. Thomas, Hydrogen adsorption on functionalized nanoporous activated carbons, J. Phys. Chem. B 109 (2005) 8880–8888, https://doi.org/10.1021/jp050080z.
[2] H. Foley, Carbogenic molecular sieves: synthesis, properties and applications, Microporous Materials 4 (6) (1995) 407–433, https://doi.org/10.1016/0927-6513(95)00014-Z.
[3] D. Siemer, J.F. Lech, R. Woodriff, Direct filtration through porous graphite for A.A. analysis of beryllium particulates in air, Spectrochim. Acta Part B At. Spectrosc. 28 (1973) 469–471, https://doi.org/10.1016/0584-8547(73)80052-7.
[5] T. Deng, X. Zhou, The preparation of porous graphite and its application in lithium ion batteries as anode material, J. Solid State Electrochem. 20 (2016) 2613–2618, https://doi.org/10.1007/s10008-016-3260-1.
[6] Y.-S. Hu, P. Adelhelm, B.M. Smarsly, S. Hore, M. Antonietti, J. Maier, Synthesis of hierarchically porous carbon monoliths with highly ordered microstructure and their application in rechargeable lithium batteries with high-rate capability, Adv. Funct. Mater. 17 (2007) 1873–1878, https://doi.org/10.1002/adfm.200601152.
[7] Y. Korenbilt, M. Rose, E. Kockrick, L. Borchardt, A. Kvit, S. Kaskel, G. Yushin, High-Rate Electrochemical Capacitors Based on Ordered Mesoporous Silicon Carbide-Derived Carbon, ACS Nano 4 (3) (2010) 1337–1344, https://doi.org/10.1021/nn901825y.
[8] M.C.A. Ferraz, Preparation of activated carbon for air pollution control, Fuel 67 (1988) 1237–1241, https://doi.org/10.1016/0016-2361(88)90045-2.
[9] T. Tay, S. Ucar, S. Karagöz, Preparation and characterization of activated carbon from waste biomass, J. Hazard Mater. 165 (2009) 481–485, https://doi.org/10.1016/J.JHAZMAT.2008.10.011.
[10] B.S. Girgis, S.S. Yunis, A.M. Soliman, Characteristics of activated carbon from peanut hulls in relation to conditions of preparation, Mater. Lett. 57 (2002) 164–172, https://doi.org/10.1016/S0167-577X(02)00724-3.
[11] V. Presser, M. Heon, Y. Gogotsi, Carbide-derived carbons - from porous networks to nanotubes and graphene, Adv. Funct. Mater. 21 (2011) 810–833, https://doi.org/10.1002/adfm.201002094.
[12] Y. Gogotsi, A. Nikitin, H. Ye, W. Zhou, J.E. Fischer, B. Yi, H.C. Foley, M.W. Barsoum, Nanoporous carbide-derived carbon with tunable pore size, Nat. Mater. 2 (2003) 591–594, https://doi.org/10.1038/nmat957.
[13] G. Yushin, E.N. Hoffman, M.W. Barsoum, Y. Gogotsi, C.A. Howell, S.R. Sandeman, G.J. Phillips, A.W. Lloyd, S.V. Mikhalovsky, Mesoporous carbide-derived carbon with porosity tuned for efficient adsorption of cytokines, Biomaterials 27 (2006) 5755–5762, https://doi.org/10.1016/J.BIOMATERIALS.2006.07.019.
[14] Y.G. Gogotsi, M. Yoshimura, Formation of carbon films on carbides under hydrothermal conditions, Nature 367 (1994) 628–630, https://doi.org/10.1038/367628a0.
[15] S. Welz, M.J. McNallan, Y. Gogotsi, Carbon structures in silicon carbide derived carbon, J. Mater. Process. Technol. 179 (2006) 11–22, https://doi.org/10.1016/J.JMATPROTEC.2006.03.103.
[16] R. Roy, D. Ravichandran, A. Badzian, E. Breval, Attempted hydrothermal synthesis of diamond by hydrolysis of β-SiC powder, Diam. Relat. Mater. 5 (1996) 973–976, https://doi.org/10.1016/0925-9635(95)00443-2.
[17] R. Riedel (Ed.), Handbook of Ceramic Hard Materials, Wiley, 2000, https://doi.org/10.1002/9783527618217.
[18] T. Kraft, K.G. Nickel, Y.G. Gogotsi, Hydrothermal degradation of chemical vapour deposited SiC fibres, J. Mater. Sci. 33 (1998) 4357–4364, https://doi.org/10.1023/A:1004480814477.
[19] Y.G. Gogotsi, Structure of carbon produced by hydrothermal treatment of β-SiC powder, J. Mater. Chem. 6 (1996) 595–604, https://doi.org/10.1039/JM9960600595.
[20] E. Rollings, G.H. Gweon, S.Y. Zhou, B.S. Mun, J.L. McChesney, B.S. Hussain, A.V. Fedorov, P.N. First, W.A. de Heer, A. Lanzara, Synthesis and characterization of atomically thin graphite films on a silicon carbide substrate, J. Phys. Chem. Solid. 67 (2006) 2172–2177, https://doi.org/10.1016/j.jpcs.2006.05.010.
[21] M. Kusunoki, M. Rokkaku, T. Suzuki, Epitaxial carbon nanotube film self-organized by sublimation decomposition of silicon carbide, Appl. Phys. Lett. 71 (1997) 2620–2622, https://doi.org/10.1063/1.120158.
[22] J. Rugolo, J. Erlebacher, K. Sieradzki, Length scales in alloy dissolution and measurement of absolute interfacial free energy, Nat. Mater. 5 (2006) 946–949, https://doi.org/10.1038/nmat1780.
[23] J. Erlebacher, M.J. Aziz, A. Karma, N. Dimitrov, K. Sieradzki, Evolution of nanoporosity in dealloying, Nature 410 (2001) 450–453, https://doi.org/10.1038/35068529.
[24] J. Erlebacher, An atomistic description of dealloying, J. Electrochem. Soc. 151 (2004) C614, https://doi.org/10.1149/1.1784820.
[25] A.J. Forty, Corrosion micromorphology of noble metal alloys and depletion gilding, Nature 282 (1979) 597–598, https://doi.org/10.1038/282597a0.
[26] H. Lechtman, Pre-Columbian Surface Metallurgy, Scientific American 250 (6) (1984) 56–63, https://doi.org/10.2307/24969389.
[27] H.W. Pickering, C. Wagner, Electrolytic dissolution of binary alloys containing a noble metal, J. Electrochem. Soc. 114 (1967) 698, https://doi.org/10.1149/1.2426709.
[28] H.W. Pickering, Volume diffusion during anodic dissolution of a binary alloy, J. Electrochem. Soc. 115 (1968) 143, https://doi.org/10.1149/1.2411048.
[29] J. Erlebacher, R.S. Guest, Hard materials with tunable porosity, MRS Bull. 34 (2009), https://doi.org/10.1557/mrs2009.155.
[30] I. McCue, A. Karma, J. Erlebacher, Pattern formation during electrochemical and liquid metal dealloying, MRS Bull. 43 (2018) 27–34, https://doi.org/10.1557/mrs.2017.301.
[31] I. McCue, E. Benn, B. Gaskey, J. Erlebacher, Dealloying and dealloyed materials, Annu. Rev. Mater. Res. 46 (2016) 263–286, https://doi.org/10.1146/annurev-matsci-070115-031739.
[32] J.D. Harrison, C. Wagner, The attack of solid alloys by liquid metals and salt melts, Acta Metall. 7 (1959) 722–735, https://doi.org/10.1016/0001-6160(59)90178-6.
[33] T. Wada, K. Yubuta, A. Inoue, H. Kato, Dealloying by metallic melt, Mater. Lett. 65 (2011) 1076–1078, https://doi.org/10.1016/J.MATLET.2011.01.054.
[34] I. McCue, B. Gaskey, B. Crawford, J. Erlebacher, Local heterogeneity in the mechanical properties of bicontinuous composites made by liquid metal dealloying, Appl. Phys. Lett. 109 (2016) 231901, https://doi.org/10.1063/1.4971776.
[35] I. McCue, B. Gaskey, P.-A. Geslin, A. Karma, J. Erlebacher, Kinetics and morphological evolution of liquid metal dealloying, Acta Mater. 115 (2016) 10–23, https://doi.org/10.1016/J.ACTAMAT.2016.05.032.
[36] B. Gaskey, I. McCue, A. Chuang, J. Erlebacher, Self-assembled porous metal-intermetallic nanocomposites via liquid metal dealloying, Acta Mater. 164 (2019) 293–300, https://doi.org/10.1016/J.ACTAMAT.2018.10.057.
[37] T. Wada, J. Yamada, H. Kato, Preparation of three-dimensional nanoporous Si using dealloying by metallic melt and application as a lithium-ion rechargeable battery negative electrode, J. Power Sources 306 (2016) 8–16, https://doi.org/10.1016/J.JPOWSOUR.2015.11.079.
[38] S.-G. Yu, K. Yubuta, T. Wada, H. Kato, Three-dimensional bicontinuous porous graphite generated in low temperature metallic liquid, Carbon N. Y. 96 (2016) 403–410, https://doi.org/10.1016/j.carbon.2015.09.093.
[39] P.-A. Geslin, I. McCue, B. Gaskey, J. Erlebacher, A. Karma, Topology-generating interfacial pattern formation during liquid metal dealloying, Nat. Commun. 6 (2015) 8887, https://doi.org/10.1038/ncomms9887.
[40] G. Cicero, G. Galli, A. Catellani, Interaction of water molecules with SiC(001) surfaces, J. Phys. Chem. B 108 (2004) 16518–16524, https://doi.org/10.1021/jp0471599.
[41] J. Stuckner, K. Frei, I. McCue, M.J. Demkowicz, M. Murayama, AQUAMI: an open source Python package and GUI for the automatic quantitative analysis of morphologically complex multiphase materials, Comput. Mater. Sci. 139 (2017) 320–329, https://doi.org/10.1016/j.commatsci.2017.08.012.
[42] M. Kusunoki, T. Suzuki, T. Hirayama, N. Shibata, K. Kaneko, A formation mechanism of carbon nanotube films on SiC(0001), Appl. Phys. Lett. 77 (2000) 531–533, https://doi.org/10.1063/1.127034.
[43] W.W. Zhong, Y.F. Huang, D. Gan, J.Y. Xu, H. Li, G. Wang, S. Meng, X.L. Chen, Wetting behavior of water on silicon carbide polar surfaces, Phys. Chem. Chem. Phys. 18 (2016) 28033–28039, https://doi.org/10.1039/C6CP04686J.
[44] Y.K. Chen-Wiegart, S. Wang, I. McNulty, D.C. Dunand, Effect of Ag–Au composition and acid concentration on dealloying front velocity and cracking during nanoporous gold formation, Acta Mater. 61 (2013) 5561–5570, https://doi.org/10.1016/J.ACTAMAT.2013.05.039.
[45] J. Räisänen, J. Hirvonen, A. Anttila, The diffusion of silicon in germanium, Solid State Electron. 24 (1981) 333–336, https://doi.org/10.1016/0038-1101(81)90027-7.
[46] H. Weis, F. Kargl, M. Kolbe, M.M. Koza, T. Unruh, A. Meyer, Self-and interdiffusion in dilute liquid germanium-based alloys, J. Phys. Condens. Matter 31 (2019), https://doi.org/10.1088/1361-648X/ab354e.
[47] H.H. Silvestri, H. Bracht, J.L. Hansen, A.N. Larsen, E.E. Haller, Diffusion of silicon in crystalline germanium, Semicond. Sci. Technol. 21 (2006) 758–762, https://doi.org/10.1088/0268-1242/21/6/008.
[48] A. Lee, R. Zhu, M. McNallan, Kinetics of conversion of silicon carbide to carbide derived carbon, J. Phys. Condens. Matter 18 (2006).
[51] D.A. Ersoy, M.J. Mcnallan, Y. Gogotsi, Carbon Coatings Produced by High Temperature Chlorination of Silicon Carbide Ceramics, 2016, https://doi.org/10.1007/s100190100136.
[52] Q. Chen, K. Sieradzki, Spontaneous evolution of bicontinuous nanostructures in dealloyed Li-based systems, Nat. Mater. 12 (2013) 1102–1106, https://doi.org/10.1038/nmat3741.
[53] G.W. Liu, M.L. Muolo, F. Valenza, A. Passerone, Survey on wetting of SiC by molten metals, Ceram. Int. 36 (2010) 1177–1188, https://doi.org/10.1016/J.CERAMINT.2010.01.001.
[54] J. Erlebacher, Mechanism of coarsening and bubble formation in high-genus nanoporous metals, Phys. Rev. Lett. 106 (2011), https://doi.org/10.1103/PhysRevLett.106.225504.
[55] F. Tuinstra, J.L. Koenig, Raman spectrum of graphite, J. Chem. Phys. 53 (1970) 1126–1130, https://doi.org/10.1063/1.1674108.
[56] N. Shimodaira, A. Masui, Raman spectroscopic investigations of activated carbon materials, J. Appl. Phys. 92 (2002) 902–909, https://doi.org/10.1063/1.1487434.

[57] M.A. Pimenta, G. Dresselhaus, M.S. Dresselhaus, L.G. Cançado, A. Jorio, R. Saito, Studying disorder in graphite-based systems by Raman spectroscopy, Phys. Chem. Chem. Phys. 9 (2007) 1276–1290, https://doi.org/10.1039/B613962K.
[58] A.C. Ferrari, J.C. Meyer, V. Scardaci, C. Casiraghi, M. Lazzeri, F. Mauri, S. Piscanec, D. Jiang, K.S. Novoselov, S. Roth, A.K. Geim, Raman spectrum of graphene and graphene layers, Phys. Rev. Lett. 97 (2006) 187401, https://doi.org/10.1103/PhysRevLett.97.187401.
[59] X. Zheng, W. Chen, G. Wang, Y. Yu, S. Qin, J. Fang, F. Wang, X.A. Zhang, The Raman redshift of graphene impacted by gold nanoparticles, AIP Adv. 5 (2015), https://doi.org/10.1063/1.4921316, 057133.
[60] X. Meng, S. Tongay, J. Kang, Z. Chen, F. Wu, S.S. Li, J.B. Xia, J. Li, J. Wu, Stable p- and n-type doping of few-layer graphene/graphite, Carbon N. Y. 57 (2013) 507–514, https://doi.org/10.1016/j.carbon.2013.02.028.
[61] W.X. Wang, S.H. Liang, T. Yu, D.H. Li, Y.B. Li, X.F. Han, The study of interaction between graphene and metals by Raman spectroscopy, American Institute of Physics, J. Appl. Phys. 109 (7) (2011), https://doi.org/10.1063/1.3536670, p. 07C501.
[62] A.C. Ferrari, Raman spectroscopy of graphene and graphite: disorder, electron-phonon coupling, doping and nonadiabatic effects, Solid State Commun. 143 (2007) 47–57, https://doi.org/10.1016/j.ssc.2007.03.052.
[63] L.G. Caṇado, K. Takai, T. Enoki, M. Endo, Y.A. Kim, H. Mizusaki, A. Jorio, L.N. Coelho, R. Magalhães-Paniago, M.A. Pimenta, General equation for the determination of the crystallite size la of nanographite by Raman spectroscopy, Appl. Phys. Lett. 88 (2006) 163106, https://doi.org/10.1063/1.2196057.
[64] B.Z. Li, Y. Wang, L. Xue, X.P. Li, W.S. Li, Acetylene black-embedded LiMn0.8-Fe0.2PO4/C composite as cathode for lithium ion battery, J. Power Sources 232 (2013) 12–16, https://doi.org/10.1016/j.jpowsour.2013.01.019.
[65] R.K. Dash, A. Nikitin, Y. Gogotsi, Microporous carbon derived from boron carbide, Microporous Mesoporous Mater. 72 (2004) 203–208, https://doi.org/10.1016/j.micromeso.2004.05.001.
[66] R.K. Dash, G. Yushin, Y. Gogotsi, Synthesis, structure and porosity analysis of microporous and mesoporous carbon derived from zirconium carbide, Microporous Mesoporous Mater. 86 (2005) 50–57, https://doi.org/10.1016/j.micromeso.2005.05.047.